

## Article

# Influence of Cerium and Nickel Co-Doping on ZnO Nanostructures for Electrochemical Behavior of H<sub>2</sub>O<sub>2</sub> Sensing Applications

Nadana Shanmugam <sup>1,†</sup>, Vedyappan Thirumal <sup>2,†</sup> , Natesan Kannadasan <sup>3,\*</sup> , Kandasamy Murugavel <sup>3</sup>, Natarajan Jayashri <sup>3</sup>, Jinho Kim <sup>2,\*</sup>  and Dongjin Choi <sup>4,\*</sup>

<sup>1</sup> Department of Physics, Dharmapuram Gnanambigai Government Arts College for Women, Nagapattinam, Mayiladuthurai 609001, Tamil Nadu, India; agilalakshmi2526@gmail.com

<sup>2</sup> Department of Mechanical Engineering, Yeungnam University, Gyeongsan 38541, Korea; thirumalvisnu@gmail.com

<sup>3</sup> Department of Physics, Sri Sarada Mahavidyalayam Arts and Science College for Women, Sarada Ashram, New Edaikkal, Ulundurpet 606107, Tamil Nadu, India; murugavel84@gmail.com (K.M.); jayashri484@gmail.com (N.J.)

<sup>4</sup> Department of Materials Science and Engineering, Hongik University, 2639-Sejong-ro, Jochiwon-eup, Sejong City 30016, Korea

\* Correspondence: nkannadasan87@gmail.com (N.K.); jinho@ynu.ac.kr (J.K.); djchoi@hongik.ac.kr (D.C.)

† These authors contributed equally to this work.



**Citation:** Shanmugam, N.; Thirumal, V.; Kannadasan, N.; Murugavel, K.; Jayashri, N.; Kim, J.; Choi, D. Influence of Cerium and Nickel Co-Doping on ZnO Nanostructures for Electrochemical Behavior of H<sub>2</sub>O<sub>2</sub> Sensing Applications. *Sustainability* **2022**, *14*, 6353. <https://doi.org/10.3390/su14106353>

Academic Editors: Balu Krishnakumar, Mani Durai and Sakthivel Kumaravel

Received: 14 April 2022

Accepted: 20 May 2022

Published: 23 May 2022

**Publisher's Note:** MDPI stays neutral with regard to jurisdictional claims in published maps and institutional affiliations.



**Copyright:** © 2022 by the authors. Licensee MDPI, Basel, Switzerland. This article is an open access article distributed under the terms and conditions of the Creative Commons Attribution (CC BY) license (<https://creativecommons.org/licenses/by/4.0/>).

**Abstract:** The present paper reports facile synthesis by simple chemical precipitation method for Zinc Oxide (ZnO) nanoparticles with cerium (Ce) and nickel (Ni) co-doped ZnO nanocrystals. The different optimum conditions are analyzed in dual metallic (Ce/Ni) nanoparticles doped with ZnO nanoparticles. Successful incorporation of cerium and nickel is predicted with X-ray diffraction (XRD) and X-ray photoelectron spectroscopy (XPS). Additionally, optical effects were studied as-prepared active materials by UV-Visible reflectance (UV-Vis-DRS) and photoluminescence (PL) measurements at room temperature. In addition, morphology investigations of the scanning electron microscope (SEM) and transmission electron microscope (TEM) are conducted. The results of electrochemical studies reveal that the co-doped product exhibits a higher H<sub>2</sub>O<sub>2</sub> sensing response, with 46.21 μA/μM.cm<sup>2</sup> for Ce/Ni-doped ZnO, which can use potentially for future biomedical applications.

**Keywords:** rare earth metal; co-dope; electrochemical; H<sub>2</sub>O<sub>2</sub> sensing

## 1. Introduction

In the recent past, materials on the nanoscale were the prime focus among researchers because of their unique physicochemical properties. ZnO is an II–IV semiconductor family with a wide bandgap of 3.34 eV [1]. The peculiar conductive, photocatalytic, piezoelectric and pyroelectric properties [2,3] of zinc oxide have made it a promising material in sensors [3,4], photovoltaic and solar cell [5,6] applications. Although numerous reports are available on doped ZnO nanostructures, there are few reports on co-doped ZnO nanocrystals [7–15]. In the current status, the exposure of hydrogen peroxide (H<sub>2</sub>O<sub>2</sub>) has gained immense significance as sensing hazards chemicals in food, bio-medical resources pharmaceuticals and the environment [16–19]. Moreover, cerium (Ce) and lanthanum (La) rare-earth metals doped ZnO nanostructures were detected the hazardous materials for biosensing applications [17–23]. Previously, few reports on ZnO nanostructures aimed at H<sub>2</sub>O<sub>2</sub> monitoring from biological targets, such as glucose, lactose and io-logical thin film samples [24,25]. The fields of study about the H<sub>2</sub>O<sub>2</sub> levels using metal oxide nanoparticles ZnO, and tin oxide (SnO<sub>2</sub>) to resolve toxic materials using electrochemical bio-sensing applications [26]. An essential assignment of Titrimetry, spectrophotometry, chemiluminescence and electrochemical methods are used and developed to detect the H<sub>2</sub>O<sub>2</sub> [27,28].

These methods, however, have certain limitations, for example, reagents are more expensive, the analysis time is lengthy, and continuing stability is very poor [29]. However, the drawbacks are rectified by using the electrochemical approaches to the measurement of  $\text{H}_2\text{O}_2$  sensing. In the field of electrochemical biosensor applications, compounds such as tin oxide ( $\text{SnO}_2$ ) [30], tungsten oxide ( $\text{WO}_2$ ) [31], copper oxide ( $\text{CuO}$ ) [32], titanium dioxide ( $\text{TiO}_2$ ) [33], magnesium oxide ( $\text{SnO}_2$ ) [34], cuprous oxide ( $\text{Cu}_2\text{O}$ ) [35] and zinc oxide ( $\text{ZnO}$ ) have demonstrated outstanding performance in the biosensor and bio-electronic sensor fields among those materials with promising behavior of metal-oxide semiconductors [36].

In this work, we report the preparation of a modified electrode of  $\text{ZnO}$  by co-doping  $\text{ZnO}$  with cerium and nickel in appropriate proportions via a facile chemical precipitation process. The personalized electrode is analyzed on behalf of its sensing activity against  $\text{H}_2\text{O}_2$ . From the obtained results, it is obvious that the modified electrode of  $\text{ZnO}$  shows higher sensor activity than bare  $\text{ZnO}$ .

## 2. Materials and Methods

### 2.1. Chemicals

Zinc acetate dihydrate [ $\text{Zn}(\text{CH}_3\text{COO})_2 \cdot 2\text{H}_2\text{O}$ ], cerium (III) chloride heptahydrate [ $(\text{CeCl}_3) \cdot 7\text{H}_2\text{O}$ ], nickel nitrate hexahydrate [ $\text{Ni}(\text{NO}_3)_2 \cdot 6\text{H}_2\text{O}$ ] and ammonium carbonate ( $(\text{NH}_4)_2\text{CO}_3$ ) are used as precursors. All the chemicals are analytical reagent grade with 99.9% purity (Sigma-Aldrich, St. Louis, MI, USA) and use without any additional purification. Sample preparation and dilutions were made of ultrapure de-ionized (DI) water.

### 2.2. Synthesis of Co-Doped $\text{ZnO}$ Nanoparticles

For the typical preparations of cerium and nickel-doped  $\text{ZnO}$ , firstly zinc acetate [ $\text{Zn}(\text{CH}_3\text{COO})_2 \cdot 2\text{H}_2\text{O}$ ] weighed 5.49g and (0.5 mol/L) was dissolved in 50 mL of deionized (DI) water with vigorous stirring by a magnetic stirrer. Additionally, a 0.05 mol/L solution of cerium (III) chloride heptahydrate [ $(\text{CeCl}_3) \cdot 7\text{H}_2\text{O}$ ], prepared in 20 mL solutions was mixed with the above the solution mixture. After 35 min, nickel nitrate hexahydrate [ $\text{Ni}(\text{NO}_3)_2 \cdot 6\text{H}_2\text{O}$ ], at different molar concentrations (0.025, 0.05, 0.075, 0.1 and 0.125 mol/L) equipped in 20 mL aqueous solution was added slowly into the above mixture of solutions. Finally, 5.64 g (1 mol/L) of  $(\text{NH}_4)_2\text{CO}_3$  in 50 mL of DI water was added gradually to the above the mixture. The entire mixture of solutions was continuously magnetic stirrer and finally until a get precipitate sediment has appeared. The obtained solid dispersions were cleaned using DI water with ethanol repeated numbers until the clear white powder was obtained. The optimized as-prepared metallic composites were dried overnight at  $80^\circ\text{C}$ . Finally, the product was treated in annealing at  $500^\circ\text{C}$  for 2 h using a box furnace. The as-prepared powders were agate mortar grinding at Pure  $\text{ZnO}$ ,  $\text{ZnO}$ : Ce (0.05 M): Ni (0.025 M),  $\text{ZnO}$ : Ce (0.05 M): Ni (0.05 M),  $\text{ZnO}$ : Ce (0.05 M): Ni (0.075 M),  $\text{ZnO}$ : Ce (0.05 M): Ni (0.1 M),  $\text{ZnO}$ : Ce (0.05 M): Ni (0.125 M). A comparable sample of pure  $\text{ZnO}$  nanocrystals was prepared under the same above experimental procedure using without the addition of Ce and Ni.

### 2.3. Material Analysis and Instrumentations

The crystalline phase and particle size of pure and co-doped  $\text{ZnO}$  electrocatalytic materials were analyzed by X-ray diffraction (XRD) measurement which was carried out at room temperature by using X'PERT-PRO, PANalytical diffractometer using  $\text{Cu K}\alpha$  radiation ( $\lambda = 1.5405 \text{ \AA}$ ). The HP 5950A Hewlett-model X-ray photoelectron spectroscopy (XPS) was examined by binding energy levels and oxidation states of  $\text{ZnO}$ , Ce and Ni. The bandgap energy of the prepared samples to be confirmed by UV-Vis NIR spectrophotometer (model: Varian-Carry 5000) at the range of 200–800 nm wavelengths in the solid barium sulfate ( $\text{BaSO}_4$ ) calibrated reference sample was made for the baseline alteration. The optical emission of the samples was recorded with a photoluminescence (PL) spectrofluorometer (Jobin Yvon, Fluorolog-FL3-11). Surface analysis micro-nano structure of the synthesized samples was done by HITACHI S-4700 scanning electron microscope (SEM)

and confirmed the depth nanostructures morphologies through JEOL-3010 transmission electron microscopy (TEM).

#### 2.4. Electrochemical Measurements

Electrochemical applications of  $\text{H}_2\text{O}_2$  sensing were carried out in a three-electrode cell set-up using a CHI-600D electrochemical workstation. The expectable three-electrode cell with a platinum wire was used as the counter electrode and Ag/AgCl (dripping wet with KCl) as the reference electrode. The as-prepared all kinds of doped and undoped binary metal nanoparticles composites were drop-casting coating with modified and polished glassy carbon electrode (GCE) with dia 3 mm) used as the working electrodes. The catalytic capability of zinc oxide toward  $\text{H}_2\text{O}_2$  reduction was employed to be evaluated by cyclic voltammetry (CV) and chronoamperometric (CA) techniques. The amperometric measurements mini magnetically stirred the constant electrolyte molar concentrations. All the kinds of electrochemical analyses were used in a phosphate buffer solution (PBS). In the direction to avoid the decomposition of  $\text{H}_2\text{O}_2$ , it was slowly mixed with the stock solution in PBS. The impedance analysis delivers details to find the resistance of the material.

### 3. Results and Discussion

#### 3.1. Structural Analysis

In Figure 1a, we have presented the X-ray diffracted patterns of pure ZnO and  $\text{Zn}_{0.95-x}\text{Ce}^{4+}_{0.05}\text{Ni}_x\text{O}$  ( $x = 0.025, 0.05, 0.075, 0.1$  and  $0.125$  M). The observed XRD patterns reveal that the samples are the hexagonal assembly of the zinc oxide (JCPDS card No: 36-1451) [15]. However, the intensity of diffraction peaks starts to reduce in the sample with  $x \leq 0.025$  M. No extra diffraction patterns follow-on from Ni or Nickel oxide can be discerned, which demonstrates the complete dispersion of the dopant. Later than a suspicious view of the XRD patterns, we calculate that the diffraction angle positions depend sensitively on the Ni concentration as shown in Figure 1b.

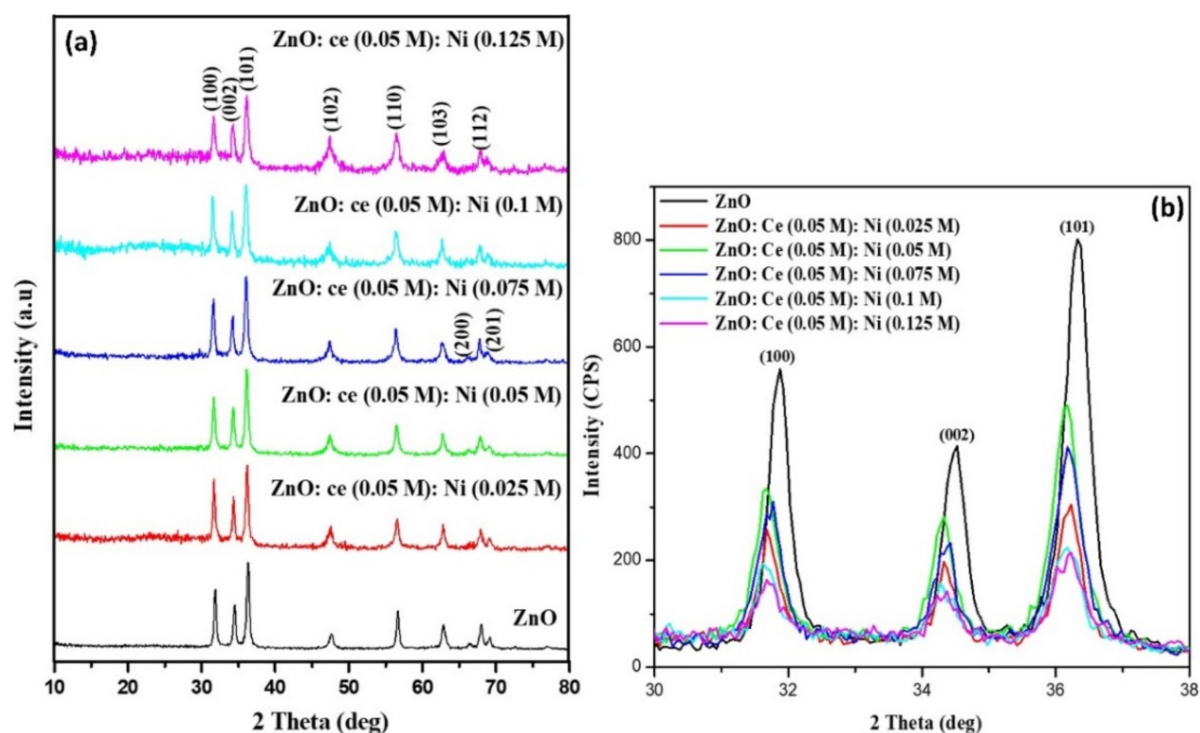


**Figure 1.** (a) XRD patterns (b) planes enlarged view of (100), (002) and (101) peaks of pure ZnO and Ce/Ni-ZnO nanoparticles.

The lattice parameters of the products started to increase nearly with increasing Ni content for the doping regions  $x \leq 0.05$  M. At  $x > 0.05$ , the lattice parameters of the products exhibit a non-monotonical varying tendency. For all the concentration of doping is in good agreement with the gained  $c/a$  values in this work. Further, the crystallite sizes estimated using Scherrer's formula exhibit a significant decrease in Ni doping as shown in Table 1.

**Table 1.** XRD derived parameters of undoped and co-doped ZnO nanoparticles.

Samples	Particle Size (nm)	Lattice Parameters (Å)		
		a = b	c	c/a
ZnO	24	3.242	5.204	1.604
ZnO: Ce (0.05 M): Ni (0.025 M)	17.99	3.257	5.220	1.602
ZnO: Ce (0.05 M): Ni (0.05 M)	16.86	3.260	5.227	1.603
ZnO: Ce (0.05 M): Ni (0.075 M)	15.85	3.256	5.224	1.604
ZnO: Ce (0.05 M): Ni (0.1 M)	14.64	3.260	5.226	1.603
ZnO: Ce (0.05 M): Ni (0.125 M)	11.19	3.256	5.224	1.604

### 3.2. XPS Analysis

Figure 2a shows significant peaks binding energy levels of Zn, Ni, Ce, O and carbon identifies using the XPS spectra of co-doped zinc oxide with 0.075 M of nickel. The depth profile XPS survey spectra of Ce, Ni, Zn, C, and O classes are displayed in parts of Figure 2b–e, respectively. The XPS binding energy (BeV) slightly appears to carbon (C1s) peak is considering reference peak C1s (285 eV). The Zn-metallic binding energies are  $2p_{3/2}$  and  $2p_{1/2}$  corresponding to strong peaks present at 1020.19 and 1043.29 eV respectively, as shown in Figure 2b, Zn  $2p_{1/2}$  with the peak centered binding energy levels at 1021 eV was due to the metallic oxide nanoparticles incorporated into ZnO in oxygen-deprived areas [22,23].

The intense peak of oxygen binding energy levels O1s at 528.88 eV was attributed to regions in ZnO shown in Figure 2c. Three peaks are identified in the Ce 3d spectrum (Figure 2d). Cerium ( $Ce^{4+}$ ) incorporated in zinc oxide, the binding energies state of  $3d_{3/2}$  and  $3d_{5/2}$ , is seen at 901.3, 908, 917 eV, and 882.6, 888.9 and 898.8 eV, respectively [36]. As shown in Figure 2e, the nickel-based binding energy  $2p_{3/2}$  is observed at 855.46 eV; however, the peak Zn  $2p_{1/2}$  is positioned binding energy at 873.1 eV. This result indicates that Ni ions in the products may have a valence of  $2^+$  [36].

### 3.3. Optical Properties

#### 3.3.1. UV-Vis Reflectance Spectroscopy

The UV-Vis spectroscopy was studied by the optical bandgap of the products between 250–750 nm. The intensity of reflectance decreases with the increase in Ni concentration. All the Ce and Ni-doped ZnO products were exhibit excellent optical properties in UV reflectance of 364–326 nm (Figure 3a). The pure ZnO and dual-metallic doped ZnO were estimated by extrapolation of the linear portion of  $(\alpha h\nu)^2$  versus  $h\nu$  curve by using the Tauc plot relation [34]. From the plot, the bandgap values are 3.4 eV 3.43, 3.50, 3.58, 3.60 and 3.72 eV of ZnO, Ce/Ni-ZnO with, 0.025, 0.05, 0.075, 0.1 and 0.125 M of nickel ions, respectively (Figure 3b).

The optical band gap values were shown in gradually increase for all the concentrations of doping samples. The principle of the Moss–Burstein band filling effect can be explained by an increase in the carrier concentration for optical energy at a wide bandgap, which is related to n-type semiconductors materials.

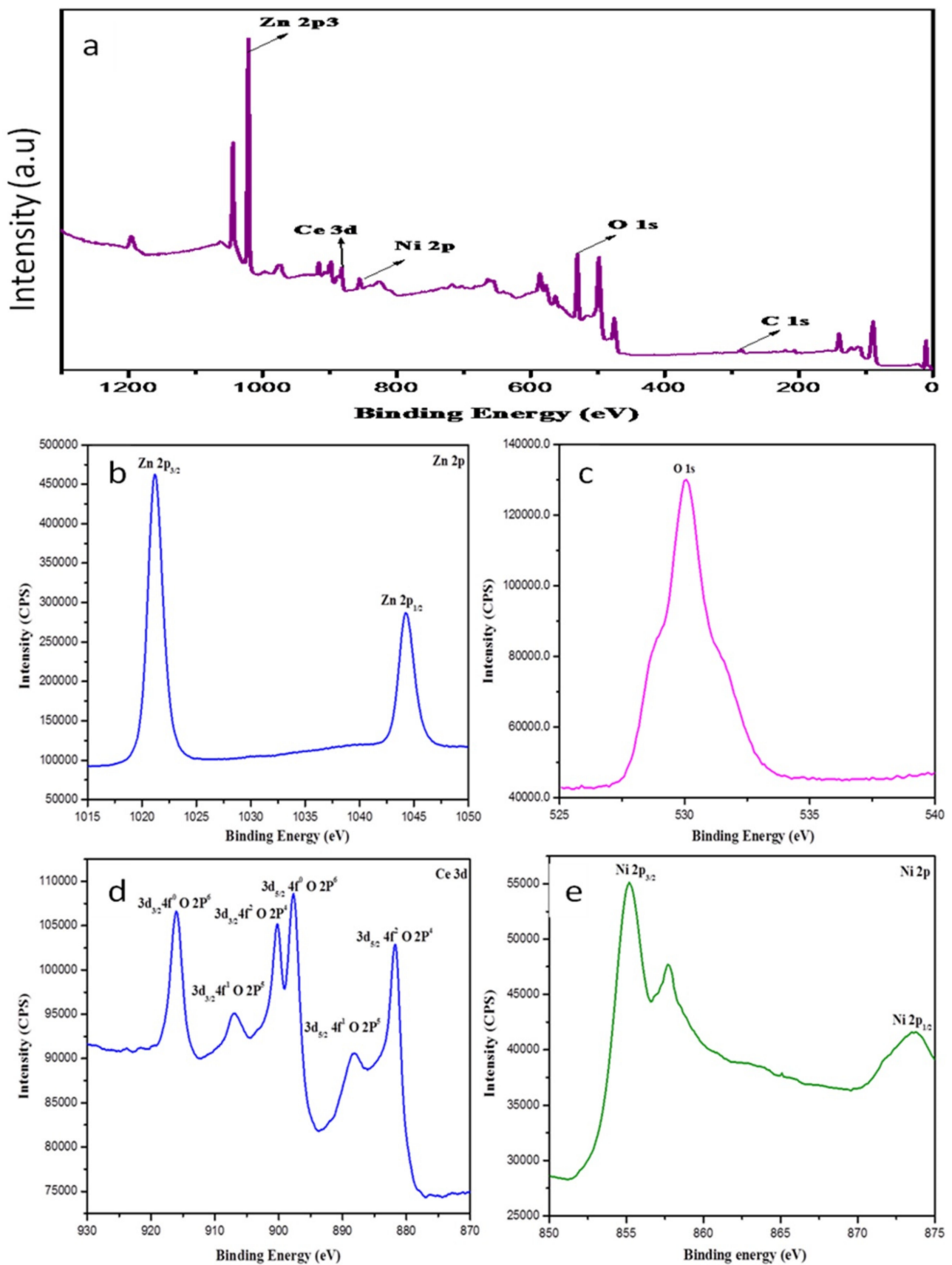


**Figure 2.** (a) XPS overall survey spectrum of Ce/Ni-doped [Ce (0.05 M), Ni (0.075 M)] ZnO nanostructures; (b–e) XPS depth profile of binding energies of Zn 2p, Ce 3d, O1s, Ni 2p.



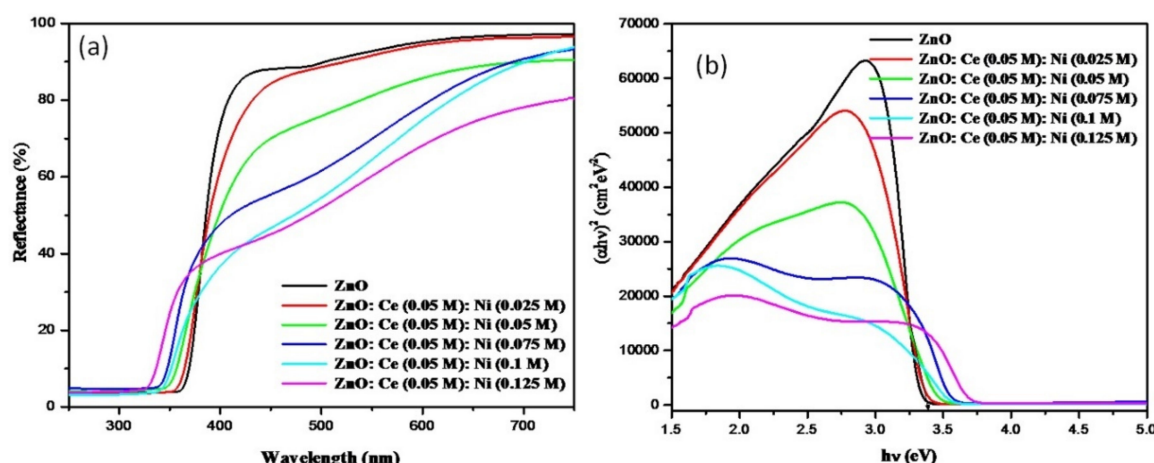


**Figure 3.** (a) UV-Vis-diffuse reflectance spectra and (b) curves of bandgap energy for pure Ce/Ni-ZnO.

### 3.3.2. Photoluminescence (PL) Analysis

The optical emission and defect formation of Pure ZnO and Ce/Ni-doping zinc oxide were examined via PL measurements. An undoped and Ce/Ni-ZnO nanoparticles PL spectra are shown in Figure 4, pure ZnO exhibits a strong UV emission at 399 nm and four weak visible emissions at 443, 465, 480 and 526 nm, respectively.

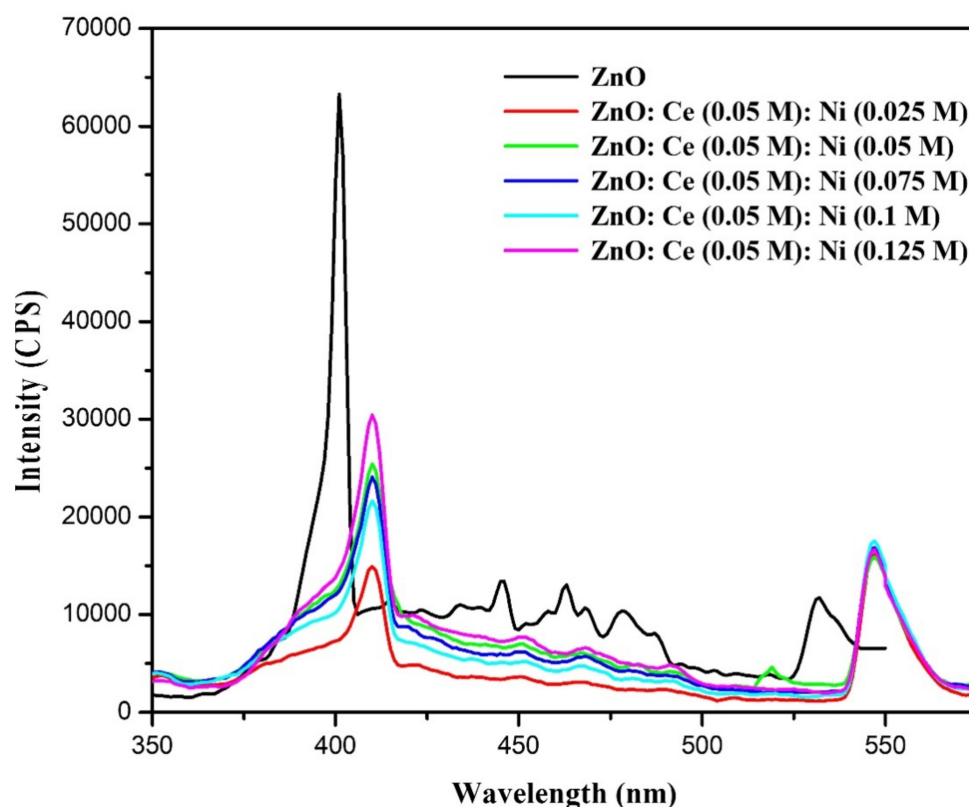


**Figure 4.** PL emission spectrum of ZnO and Ce/Ni-ZnO nanostructures.

The strong and narrow UV emission at 399 nm is recognized as the near band edge emission of ZnO, originating from the excitonic transitions among the electrons in the conduction bands and the holes in the valence bands [37]. However, all the ZnO and Ce/Ni-ZnO samples displayed only one in the UV region (410 nm) and the others in the visible region (545 nm), which can be attributed to the single-ionized oxygen vacancies [38].

It is observed that the UV emission peaks are red-shifted with intensity quenching following an increase in Ni content. The non-radiative recombination of excitons wavelengths can be credited to intensity quenching. Alternatively, all the co-doped products exhibit intense visible emission at 537 nm compared to undoped ZnO, signifying the doping-concentration dependable point defects multi peak PL emission ranging from blue region to red region identical co-existence of interstitial zinc ( $Zn_i$ ) and zinc vacancy ( $V_{Zn}$ ).

### 3.4. FT-IR Analysis

FT-IR spectra of pure ZnO compared to dual-doped ZnO nanoparticles are shown in Figure 5. IR transmittance peaks at around  $428\text{ cm}^{-1}$  associated with the stretching bond, which confirms that the octahedral coordination shows the FT-IR spectrum of ZnO. On co-doping, stretching vibrations of ZnO were broadened and shifted to higher frequencies following increases in Ce, Ni dual-doping concentration in ZnO. The appreciable shifts in the frequency with nickel (Ni) doping concentration are caused by differences in the band lengths that occur when  $Ni^{2+}$  ions substitute into  $Zn^{2+}$  ions in the ZnO crystal lattice. The wide absorption band appearing at about  $3431$  and  $1631\text{ cm}^{-1}$  could be ascribed to the O-H stretching, respectively. All the doped products exhibit few addition bands at around  $1514$ ,  $1385$ ,  $1018$  and  $858\text{ cm}^{-1}$ . The absorption band appearing at  $1514\text{ cm}^{-1}$  was credited to  $CO_2$  for asymmetric stretching vibration. The existence of an absorption peak located at  $1385\text{ cm}^{-1}$  is observed in ammonium ion angular distribution. A stretching vibration mode of C=C and O-C-O bonds in acetate ions absorption band at around  $1018\text{ cm}^{-1}$ . Additionally,  $854\text{ cm}^{-1}$  may be ascribed to the C-H bending plane's broad and visible appearance.

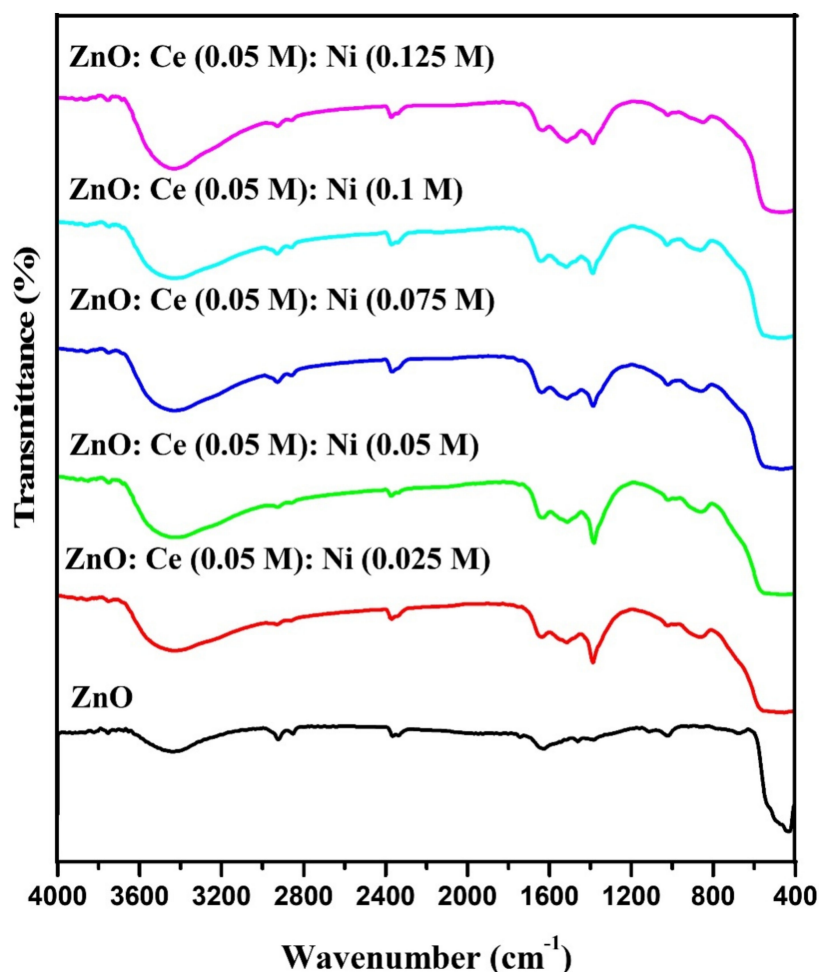
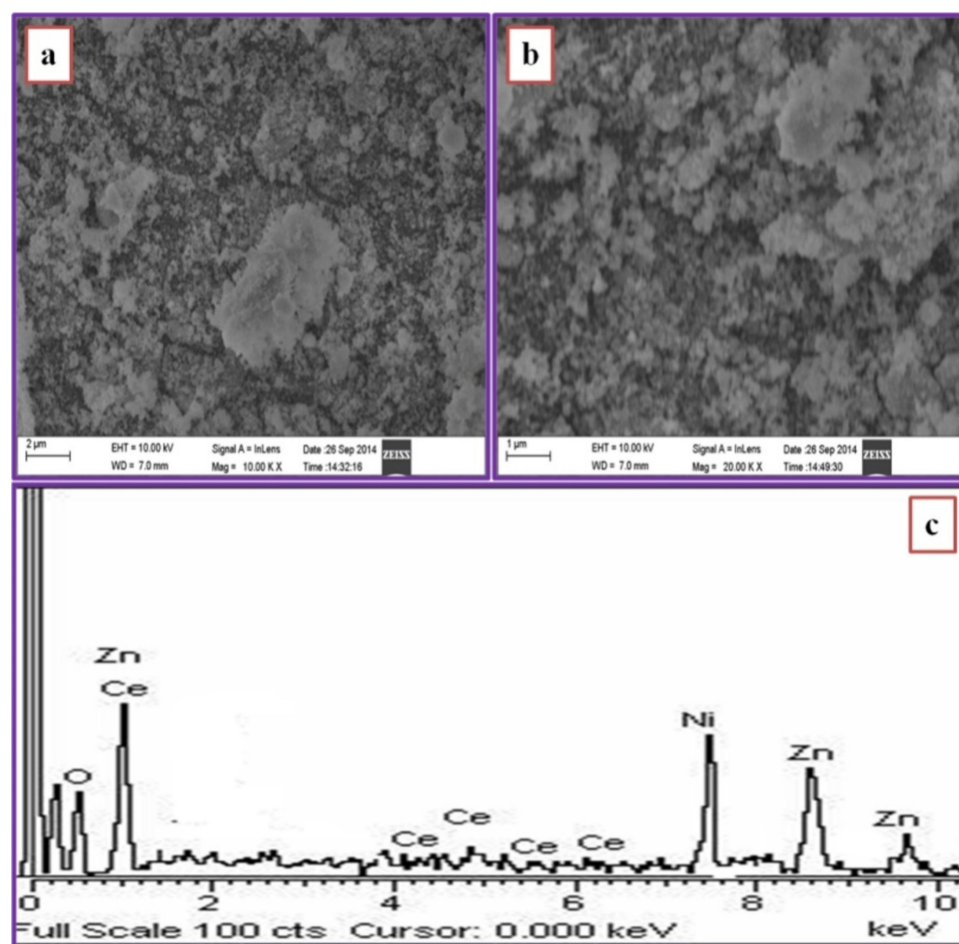


Figure 5. FT-IR spectra of pure and Ce/Ni-ZnO nanostructures.

### 3.5. Morphological Characterization

Figure 6a,b shows FE-SEM morphologies of the dual-doped ZnO with Ni concentration 0.075 M analyzed. The FE-SEM images reveal a densely populated spherical particle with a typical dia at <100 nm. The elemental composition indexed by EDX analysis confirms the presence of dopant ions cerium and nickel (Figure 6c).



**Figure 6.** (a,b) FE-SEM images of Ce/Ni-ZnO [ $\text{Ce}^{4+}$  (0.05 M) and Ni ions (0.075 M)] composite nanostructures, (c) corresponding EDX pattern.

To ascertain the high resolutions, morphological HR-TEM was recorded for pure ZnO and co-doping samples, Figure 7a shows the HR-TEM image of co-doped ZnO. As shown in the HR-TEM image, the structural patterns are identical to the undoped ZnO, revealing that the co-doping does not alter the actual hexagonal structure of ZnO. The TEM image of co-doped ZnO exhibits size in the range of 15–20 nm spherical particles with partially agglomerated (Figure 7b). The selected area diffracted patterns (SEAD) are distinct circular rings that show a co-doped ZnO pattern of a crystalline nature (Figure 7c).

### 3.6. Electrochemical Characterization

The electrochemical sensitivity of hydrogen-peroxide aims to apply as-prepared pure ZnO and co-doped Ce-Ni doped ZnO nanostructures as active electrode materials toward  $\text{H}_2\text{O}_2$  sensing over the electro-reduction process. The electrochemical analysis of cyclic voltammetry (CVs) was recorded at various sweep rates of 50–500 mV/s with  $\text{H}_2\text{O}_2$  in 2 mM  $\text{C}_6\text{N}_6\text{FeK}_3$  with a mixture of 0.5 M, KCl solution. From the CV curves, it is observed that a pair of redox peaks is clearly seen for all sweep rates, revealing the pseudocapacitance behavior.



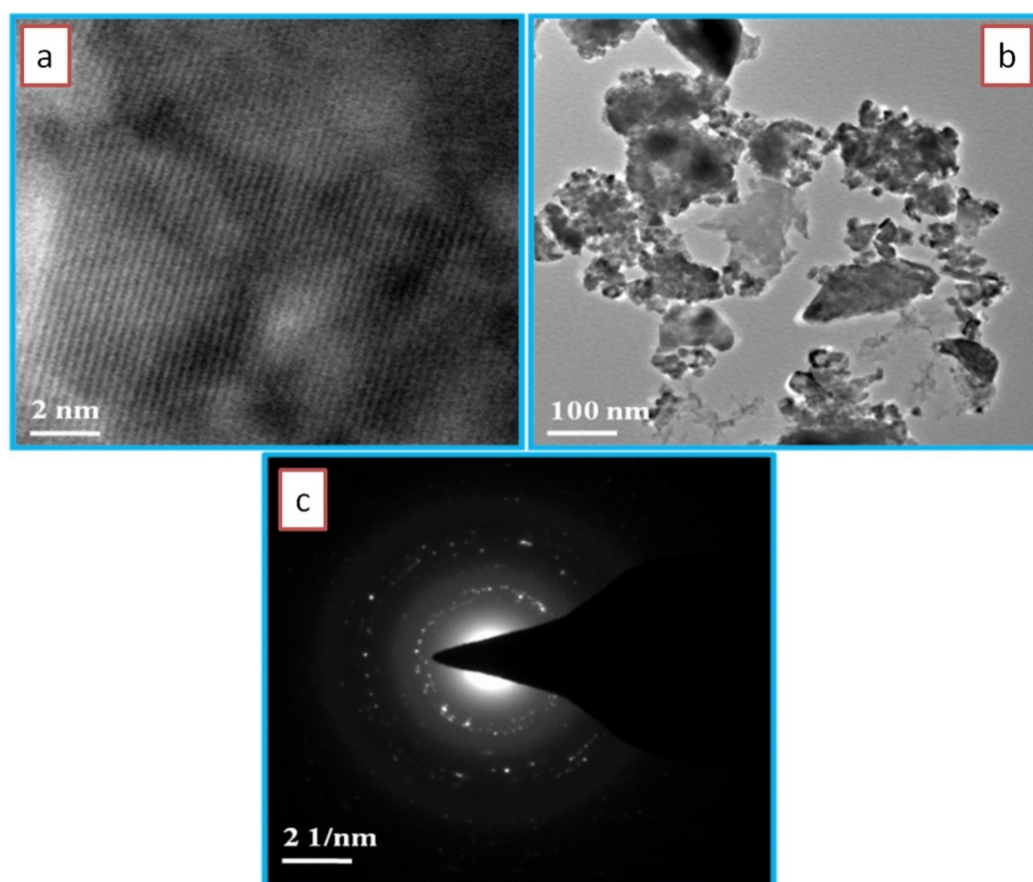


**Figure 7.** (a) HR-TEM micrographs of Ce/NiZnO [Ce (0.05 M) and Ni (0.075 M)] nanostructures, (b) consistent HR-TEM images and (c) SAED pattern.

Figure 8a,b presents the CV curvatures of pure ZnO and Ce/Ni- ZnO, the reduction of ZnO into  $\text{Zn}^{2+}$  reveals that cathodic peaks and the formation of ZnO demonstrate anodic peaks. The anodic and cathodic peaks were increased and, when increased the scan/sweep rate ( $\text{mV/s}$ ) increased, the redox shape of the CV curves changed respectively. The Ce/Ni-ZnO electrode shows a higher peak current and high electrochemical active area, associated with undoped ZnO. Consequentially, the improvement of reaction kinetics and better electrode utilization resulted from the square root of sweep rate ( $\text{mV/s}$ )<sup>2</sup>, which is favorable in the  $\text{H}_2\text{O}_2$  sensor applications for our doped-active materials. The peak current ( $I_p$ ) increased linearly both in the anodic and cathodic directions ( $R^2 = 0.99$ ) (here,  $R^2$  is scan/sweep rate ( $\text{mV/s}$ )<sup>2</sup>), as indicated in Figure 8c.

### 3.7. Electrochemical Impedance Spectroscopy (EIS)

In order to ascertain the feasibility of the as-prepared dual-doped electrode for electrode active materials and electro-electrolyte charge transfer resistance ( $R_{ct}$ ) measurement, the electrochemical impedance spectra were recorded for both un-doped and co-doped electrodes of pure ZnO, as shown Figure 9a,b. The EIS spectra show both pure ZnO and Ce/Ni-doped ZnO electrodes in the high-frequency region at the semicircular arc and low-frequency straight line the Warburg impedance ( $W_\Omega$ ). The measurement from the EIS spectrum is  $R_{ct}$ -295  $\Omega$ , whereas it is reduced to  $R_{ct}$ -6.25  $\Omega$  for active electrode materials of co-doped ZnO, suggesting it has low resistance and is a good potential candidate for electro-catalytic  $\text{H}_2\text{O}_2$  sensing applications.

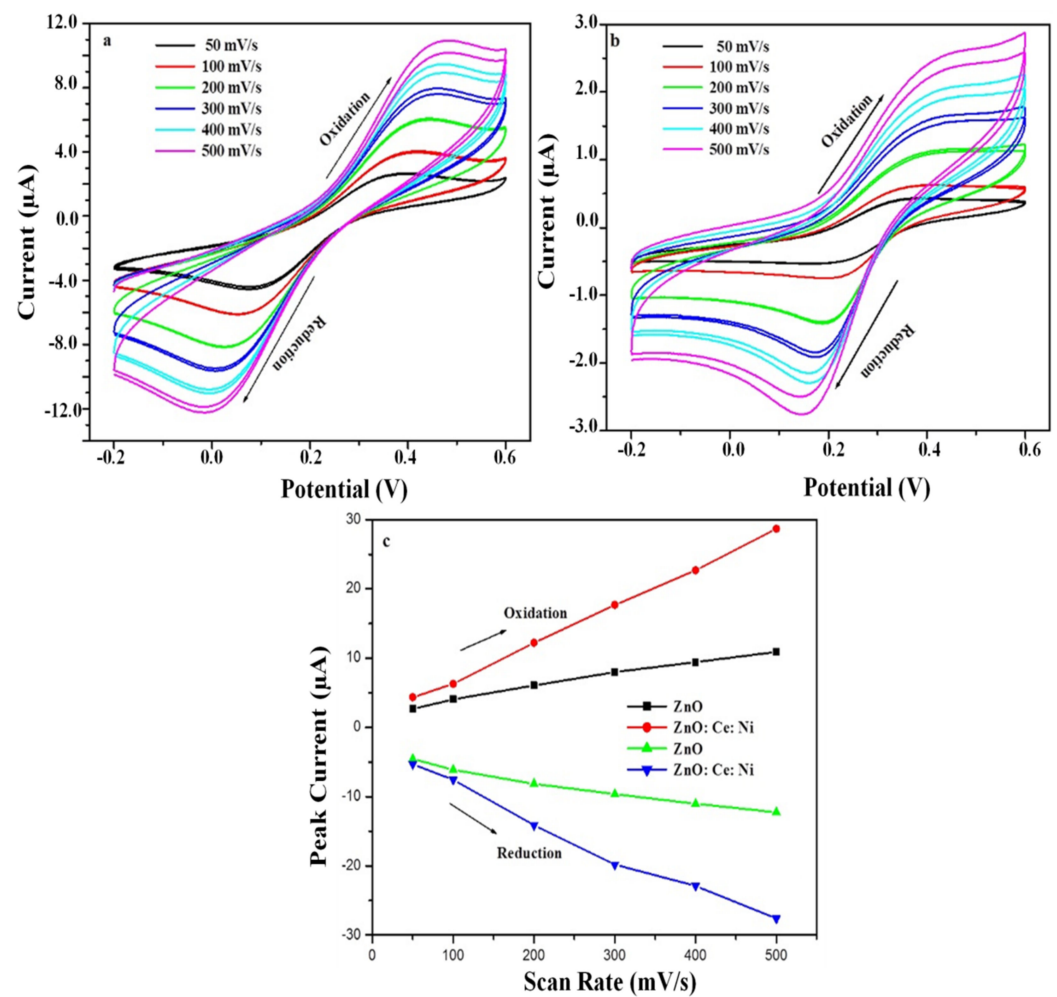


**Figure 8.** (a,b) Cyclic voltammetry curves of Ce/Ni-ZnO [ $\text{Ce}^{4+}$  0.05 M] & Ni (0.075 M) active electrodes in 2 mM,  $\text{K}_3[\text{Fe}(\text{CN})_6]$  with 0.5 M KCl electrolyte solution at different sweep rates. (c) Plots for square root of sweep rate versus peak currents intended for oxidation and reduction.

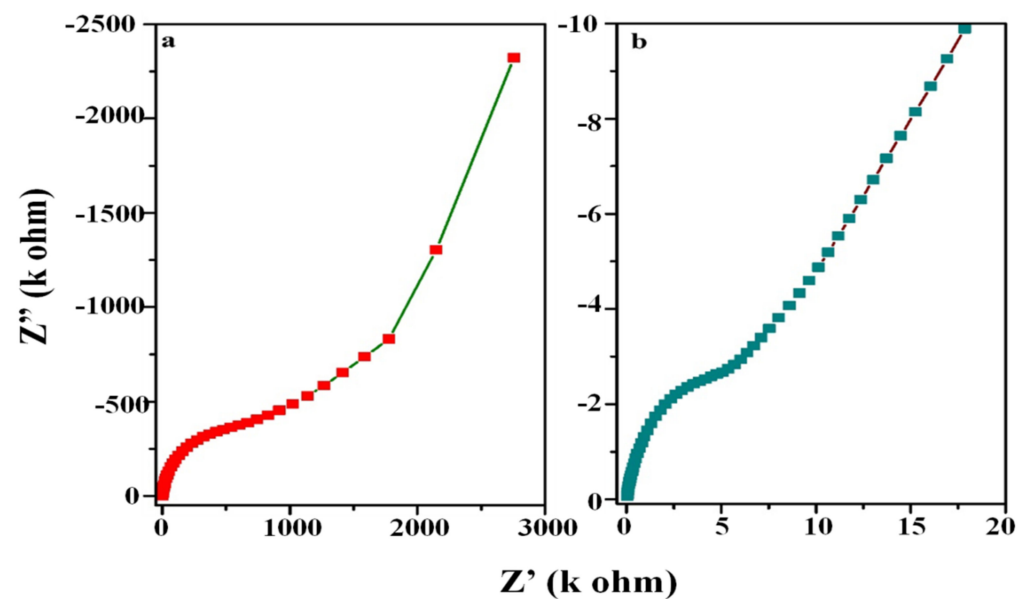


**Figure 9.** (a,b) EIS spectra of ZnO and Ce/Ni-ZnO [ $\text{Ce}$ (0.05 M) and  $\text{Ni}$ (0.075 M)] electrode.

### 3.8. Electrochemical Performance of Bare and Ce/Ni-ZnO for $H_2O_2$ Sensing

The electrocatalytic sensing of the amperometric detection method at various concentrations upon successive addition of  $H_2O_2$  of the pure ZnO electrode and Ce/Ni-doped ZnO electrode were investigated, as shown in Figure 10a,b respectively. Figure 10 shows a rapid rise in step current upon the addition of  $H_2O_2$ , equally evident in un-doped and Ce/Ni-doped electrodes of ZnO. The calibration curves the cathodic current rise depending on the concentration of hydrogen peroxide in both the cases of electrodes, as shown in Figure 10c,d.

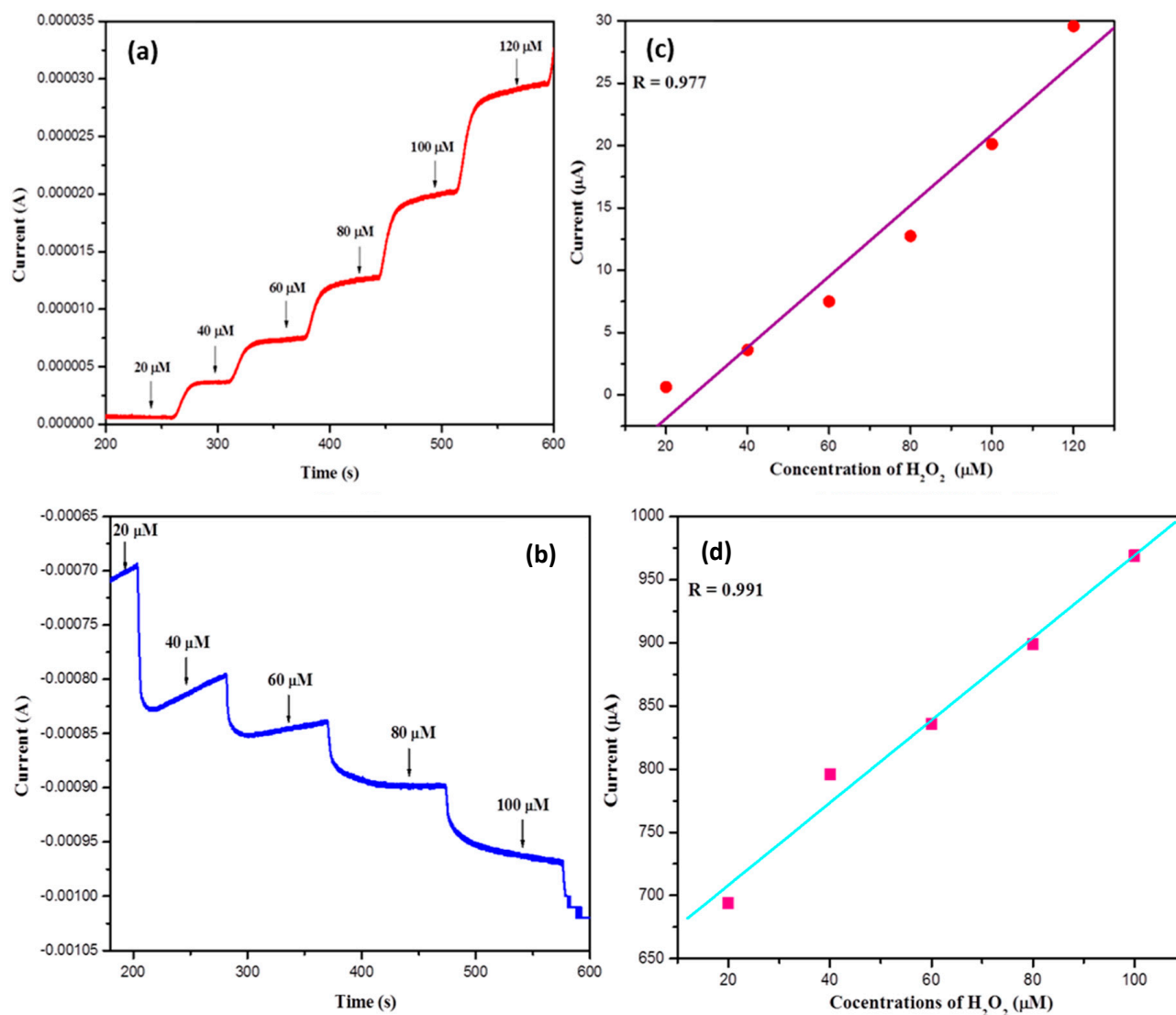


**Figure 10.** Amperometric measurements for (a) undoped, (b) Ce/Ni-ZnO [ $Ce^{4+}$  (0.05 M) and Ni (0.075 M)] with  $H_2O_2$  into 0.1 M of KCl, (c,d) consistent linear graph of sensing current (A) versus  $H_2O_2$  concentrations.

The amperometric current vs. time detection of  $H_2O_2$  values at 0.979 and 0.991 are correlation coefficients of bare zinc oxide and Ce/Ni-doped ZnO electrodes, respectively. Based on the amperometric current indication ratio of 3.0 and pure ZnO and  $H_2O_2$  sensor, these exhibit a detection with the border of 26.92  $\mu M$  from the projected slope of the curve, and its sensitivity is 3.686  $\mu A/\mu M.cm^2$ . However, a finding perimeter of 15.89  $\mu M$  is observed; in addition,  $H_2O_2$  sensitivity is 46.21  $\mu A/\mu M.cm^2$ , corresponding to the Ce/Ni-ZnO materials. Many researchers have reported biosensing applications based on ZnO nanoparticles with a reduction of  $H_2O_2$  [38,39].

#### 4. Conclusions

We have successfully developed an electrocatalytic-amperometric detection technique for  $\text{H}_2\text{O}_2$  sensor applications using pure ZnO and cerium and nickel co-doped ZnO nanoparticles. The electrocatalytic active materials were cerium and nickel-doped ZnO synthesized via a facile chemical precipitation technique, and their structural and morphological structures were analyzed. The XRD examination to find the wurtzite phase of zinc oxide confirms structural analysis for all concentrations of Ce and Ni incorporation. With an increase in nickel (Ni) concentration, the photo-luminescence spectrum of Ce/Ni-ZnO showed that the UV spectrum suppressed and improved defects related to the green emission region. The grain sizes decreased with co-doped samples showing the morphological analyses. Finally, we achieved a good current response amperometric (I) vs. time (s) detection of  $\text{H}_2\text{O}_2$ . In addition, the sensitivity is  $46.21 \mu\text{A}/\mu\text{M}\cdot\text{cm}^2$  and obtains the concentration range of  $15.89 \mu\text{M}$  for the modified electrode of Ce/Ni-doped ZnO. The Ce/Ni-ZnO electrode gives higher sensory  $\text{H}_2\text{O}_2$  detection activity than the pure ZnO. This result indicates that dual-doped ZnO nanostructures exhibit good response for future electrochemical sensing applications.

**Author Contributions:** First authors N.S. and V.T. equally contributed to the paper. N.S. and V.T. conceived the presented idea and processed the experimental data writing. K.M. and N.J. performed the analysis and drafted the manuscript with data collections. N.K. worked on the technical details, designed the figures, and wrote the manuscript. J.K., contributed to project administration and funding acquisition. D.C. contributed to conceptualization, investigation, writing, project administration, and funding acquisition. All authors have read and agreed to the published version of the manuscript.

**Funding:** This work has supported by the National Research Foundation of Korea (NRF) grant funded by the Korea government (MSIT) (No: 2022R1A2C1005357), and this research was funded by International Science & Business Belt support program, through the Korea Innovation Foundation funded by the Ministry of Science and ICT (No: 1711149716).

**Institutional Review Board Statement:** Not applicable.

**Conflicts of Interest:** The authors declare no conflict of interest.

#### References

1. Hammad, T.M.; Salem, J.K. Synthesis and characterization of Mg-doped ZnO hollow spheres. *J. Nanopart. Res.* **2011**, *13*, 2205–2212. [\[CrossRef\]](#)
2. Xu, C.X.; Sun, X.W.; Zhang, X.H.; Ke, L.; Chua, S.J. Photoluminescent properties of copper-doped zinc oxide nanowires. *Nanotechnology* **2004**, *15*, 856. [\[CrossRef\]](#)
3. Klingshirn, C. ZnO: Material, Physics and Applications. *ChemPhysChem* **2007**, *8*, 782–803. [\[CrossRef\]](#) [\[PubMed\]](#)
4. Wang, Z.L.; Song, J.H. Piezoelectric Nanogenerators Based on Zinc Oxide Nanowire Arrays. *Science* **2006**, *312*, 242. [\[CrossRef\]](#) [\[PubMed\]](#)
5. Huang, G.J.; Wang, J.B.; Zhong, X.L.; Zhou, G.C.; Yan, H.L. Synthesis, structure, and room-temperature ferromagnetism of Ni-doped ZnO nanoparticles. *J. Mater. Sci.* **2007**, *42*, 6464–6468. [\[CrossRef\]](#)
6. Chen, Y.; Ding, M.H.; Sun, S. Preparation and Characterization of ZnO Nanoparticles Supported on Amorphous  $\text{SiO}_2$ . *Nanomaterials* **2017**, *7*, 217. [\[CrossRef\]](#)
7. Seetha, M.; Bharathi, S.; Raj, A.D.; Mangalaraj, D.; Nataraj, D. Optical investigations on indium oxide nano-particles prepared through precipitation method. *Mater. Charact.* **2009**, *60*, 1578–1582. [\[CrossRef\]](#)
8. Zhang, Z.Y.; Bao, C.G.; Yao, W.J.; Ma, S.Q.; Zhang, L.L.; Hou, S.Z. Influence of deposition temperature on the crystallinity of Al-doped ZnO thin films at glass substrates prepared by RF magnetron sputtering method. *Superlattices Microstruct.* **2011**, *49*, 644–653. [\[CrossRef\]](#)
9. Gu, H.; Jiang, Y.; Yan, M. Defect-induced room temperature ferromagnetism in Fe and Na co-doped ZnO nanoparticles. *J. Alloy. Compd.* **2012**, *521*, 90. [\[CrossRef\]](#)
10. Li, H.; Zhang, Z.; Huang, J.; Liu, R.; Wang, Q. Optical and structural analysis of rare earth and Li co-doped ZnO nanoparticles. *J. Alloy. Compd.* **2013**, *550*, 526. [\[CrossRef\]](#)
11. Bai, Y.F.; Wang, Y.X.; Yang, K.; Zhang, X.R.; Song, Y.L. Enhanced upconverted photoluminescence in  $\text{Er}^{3+}$  and  $\text{Yb}^{3+}$  codoped ZnO nanocrystals with and without  $\text{Li}^+$  ions. *Opt. Commun.* **2008**, *281*, 5448. [\[CrossRef\]](#)

12. Lang, J.H.; Lia, X.; Yang, J.H.; Yang, L.L.; Zhang, Y.J.; Yan, Y.S.; Han, Q.; Wei, M.B.; Gao, M.; Liu, X.Y.; et al. Rapid synthesis and luminescence of the  $\text{Eu}^{3+}$ ,  $\text{Er}^{3+}$  co-doped ZnO quantum-dot chain via chemical precipitation. *Appl. Surf. Sci.* **2011**, *257*, 9574. [\[CrossRef\]](#)
13. Tamilalagan, E.; Selvi, S.V.; Chen, S.-M.; Akilarasan, M.; Maheshwaran, S.; Chen, T.-W.; Al-Mohaimed, A.M.; Al-Onazi, W.A.; Elshikh, M.S.; Liu, X. Fabrication of p-n Junction (Ni/Zn)O and Reduced Graphene Oxide (rGO) Nanocomposites for the Electrocatalysis of Analgesic Drug (Acetaminophen) Detection in Pharmaceutical and Biological Samples. *J. Electrochem. Soc.* **2021**, *168*, 036501. [\[CrossRef\]](#)
14. Renganathan, V.; Balaji, R.; Chen, S.M.; Kogularasu, S.; Akilarasan, M. Bifunctional bimetallic heterojunction material based on  $\text{Al}_2\text{O}_3/\text{ZnO}$  micro flowers for electrochemical sensing and catalysis. *Ecotoxicol. Environ. Saf.* **2019**, *176*, 250–257. [\[CrossRef\]](#) [\[PubMed\]](#)
15. Kogularasu, S.; Akilarasana, M.; Chena, S.-M.; Chena, T.-W.; Lou, B.-S. Urea-based morphological engineering of ZnO; for the biosensing enhancement towards dopamine and uric acid in food and biological samples. *Mater. Chem. Phys.* **2019**, *227*, 5–11. [\[CrossRef\]](#)
16. D'Alessandro, A.; Coffetti, D.; Crotti, E.; Coppola, L.; Meoni, A.; Ubertini, F. Self-Sensing Properties of Green Alkali-Activated Binders with Carbon-Based Nanoinclusions. *Sustainability* **2020**, *12*, 9916. [\[CrossRef\]](#)
17. Iqbal, J.; Liu, X.F.; Zhu, H.C.; Wu, Z.B.; Zhang, Y.; Yu, D.P.; Yu, R.H. Raman and highly ultraviolet red-sifted near band edge properties of LaCe co-doped ZnO nanoparticles. *Acta Mater.* **2009**, *57*, 4790. [\[CrossRef\]](#)
18. Tana, W.K.; Razak, K.A.; Lockman, Z.; Kawamura, G.; Muto, H.; Matsuda, A. Photoluminescence properties of rod-like Ce-doped ZnO nanostructured films formed by hot-water treatment of sol-gel derived coating. *Opt. Mater.* **2013**, *35*, 1902. [\[CrossRef\]](#)
19. Ri, K.H.; Wang, Y.B.; Zhou, W.L.; Gao, J.X.; Wang, X.J.; Yu, J. The structural properties of Al-doped ZnO films depending on the thickness and their effect on the electrical properties. *Appl. Surf. Sci.* **2011**, *258*, 1283. [\[CrossRef\]](#)
20. Shin, B.K.; Lee, T.I.; Kar, J.P.; Lee, M.J.; Park, K.I.; Ahn, K.J.; Yeom, K.Y.; Cho, J.H.; Myoung, J.M. Effect of deposition power on structural and electrical properties of Al-doped ZnO films using pulsed direct-current magnetron sputtering with single cylindrical target. *Mat. Sci. Semicon. Proc.* **2011**, *14*, 23. [\[CrossRef\]](#)
21. Lin, J.-C.; Peng, K.-C.; Yeh, T.-Y.; Lee, S.-L. On the Structure and Characterization of Al, Sc-Co-Doped ZnO-Films Varying with 0–2.37 wt.% Sc Contents. *Thin Solid Film.* **2009**, *517*, 4715. [\[CrossRef\]](#)
22. Larachi, F.; Pierre, J.; Adnot, A.; Bernis, A. Ce 3d XPS study of composite  $\text{CexMn}_{1-x}\text{O}_{2-y}$  wet oxidation catalysts. *Appl. Surf. Sci.* **2002**, *195*, 236. [\[CrossRef\]](#)
23. Galtayries, A.; Blanco, G.; Cifredo, G.A.; Finol, D.; Gatica, J.M.; Pintado, J.M. XPS Analysis and Microstructural Characterization of a Ce/Tb Mixed Oxide Supported on a Lanthana-modified Transition Alumina. *Surf. Interface Anal.* **1999**, *27*, 941. [\[CrossRef\]](#)
24. Wang, J.; Xu, M.; Zhao, R.; Chen, G. A highly sensitive  $\text{H}_2\text{O}_2$  sensor based on zinc oxide nanorod arrays film sensing interface. *Analyst* **2010**, *135*, 1992–1996. [\[CrossRef\]](#) [\[PubMed\]](#)
25. Liu, J.; Li, Y.; Huang, X.; Zhu, Z. Tin Oxide Nanorod Array-Based Electrochemical Hydrogen Peroxide Biosensor Biosens. *Nanoscale Res. Lett.* **2010**, *5*, 1177–1181. [\[CrossRef\]](#) [\[PubMed\]](#)
26. Komazaki, Y.; Inoue, T.; Tanaka, S. Automated measurement system for  $\text{H}_2\text{O}_2$  in the atmosphere by diffusion scrubber sampling and HPLC analysis of Ti(IV)-PAR- $\text{H}_2\text{O}_2$  complex. *Analyst* **2001**, *5*, 587–593. [\[CrossRef\]](#) [\[PubMed\]](#)
27. Gao, P.; Liu, D. Facile synthesis of copper oxide nanostructures and their application in non-enzymatic hydrogen peroxide sensing. *Sens. Actuators B Chem.* **2015**, *208*, 346–354. [\[CrossRef\]](#)
28. Sivalingam, D.; Gopalakrishnan, J.B.; Krishnan, U.M.; Madanagurusamy, S.; Rayappan, J.B.B. Nanostructured ZnO thin film for hydrogen peroxide sensing. *Phys. E Low Dimens. Syst. Nanostruct.* **2011**, *43*, 1804–1808. [\[CrossRef\]](#)
29. Deng, Z.; Gong, Y.; Luo, Y.; Tian, Y.  $\text{WO}_3$  nanostructures facilitate electron transfer of enzyme: Application to detection of  $\text{H}_2\text{O}_2$  with high selectivity. *Biosens. Bioelectron.* **2009**, *24*, 2465–2469. [\[CrossRef\]](#)
30. Fratoddi, I.; Macagnano, A.; Battocchio, C.; Zampetti, E.; Venditti, I.; Russo, M.V.; Bearzotti, A. Platinum nanoparticles on electrospun titania nanofibers as hydrogen sensing materials working at room temperature. *Nanoscale* **2014**, *6*, 9177–9184. [\[CrossRef\]](#)
31. Zhao, J.; Qin, L.; Hao, Y.; Guo, Q.; Mu, F.; Yan, Z. Application of tubular tetrapod magnesium oxide in a biosensor for hydrogen peroxide. *Microchim. Acta* **2012**, *178*, 439–445. [\[CrossRef\]](#)
32. Xu, F.; Deng, M.; Li, G.; Chen, S.; Wang, L. Electrochemical behavior of cuprous oxide-reduced graphene oxide nanocomposites and their application in nonenzymatic hydrogen peroxide sensing. *Electrochim. Acta* **2013**, *88*, 59–65. [\[CrossRef\]](#)
33. Al-Hardan, N.H.; Jalar, A.; Hamid, M.A.A.; Keng, L.K.; Shamsudin, R.; Majlis, B.Y. The room-temperature sensing performance of ZnO nanorods for 2-methoxyethanol solvent. *Sens. Actuators B Chem.* **2014**, *203*, 223–228. [\[CrossRef\]](#)
34. Kannadasan, N.; Shanmugam, N.; Cholan, S.; Sathishkumar, K.; Poonguzhali, R.; Viruthagiri, G. Synergistic effect of bimetal ions (Ce, Pb) incorporation on optical, structural, and sensory activity of ZnO nanocrystals. *J. Solid State Electrochem.* **2015**, *19*, 757–768. [\[CrossRef\]](#)
35. Zhang, Y.; Bai, X.; Wang, X.; Shiu, K.-K.; Zhu, Y.; Jiang, H. Highly sensitive graphene-Pt nanocomposites amperometric biosensor and its application in living cell  $\text{H}_2\text{O}_2$  detection. *Anal. Chem.* **2014**, *86*, 9459. [\[CrossRef\]](#)
36. Xu, C.X.; Zhu, G.P.; Li, X.; Yang, Y.; Tan, S.T.; Sun, X.W.; Smith, T.A. Growth and spectra analysis of ZnO nanotubes. *J. Appl. Phys.* **2008**, *103*, 094303–094305. [\[CrossRef\]](#)



37. Zheng, Y.; Wang, Z.; Peng, F.; Fu, L. Application of biosynthesized ZnO nanoparticles on an electrochemical H<sub>2</sub>O<sub>2</sub> biosensor. *Braz. J. Pharm. Sci.* **2016**, *52*, 781–786. [[CrossRef](#)]
38. Aydoğdu, G.; Zeybek, D.K.; Pekyardımcı, Ş.; Kılıç, E. A novel amperometric biosensor based on ZnO nanoparticles-modified carbon paste electrode for determination of glucose in human serum. *Artif. Cells Nanomed. Biotechnol.* **2013**, *41*, 332–338. [[CrossRef](#)]
39. Zhu, X.; Yuri, I.; Gan, X.; Suzuki, I.; Li, G. Electrochemical study of the effect of nano-zinc oxide on microperoxidase and its application to more sensitive hydrogen peroxide biosensor preparation. *Biosens. Bioelectron.* **2007**, *22*, 1600–1604. [[CrossRef](#)]